JOURNAL OF GEOPHYSICAL RESEARCH, VOL. 108, NO. D20, 4626, doi:10.1029/2003JD003401, 2003

On the angular radiance closure of tropical cumulus congestus clouds observed by the Multiangle Imaging Spectroradiometer

Paquita Zuidema
NOAA Environmental Technology Laboratory, Boulder, Colorado, USA

Roger Davies and Catherine Moroney
Jet Propulsion Laboratory, California Institute of Technology, Pasadena, California, USA

Received 10 January 2003; revised 5 July 2003; accepted 29 July 2003; published 17 October 2003.

[1] Monte Carlo reflectance simulations of three tropical cumulus congestus clouds reconstructed from Multiangle Imaging Spectroradiometer (MISR) data are compared to the domain-averaged MISR reflectance measurements. The goal of the comparison is to evaluate the nadir-view pixel cloud optical depth retrievals derived using plane-parallel radiative transfer theory, and the assumptions for vertically distributing the optical depth. Cloud heights are operationally retrieved using a stereo-imaging algorithm. The cloud heights and optical depths are at a 275 m spatial resolution, and for most simulations a vertical resolution of 250 m is applied. Five different but common three-dimensional cloud representations are assessed, using (1) a column vertical-mean volume extinction coefficient (β) value (the reference case), (2) a volume extinction coefficient proportional to the two-thirds power of height (the adiabatic assumption), (3) the adiabatic assumption at a 25 m vertical resolution, (4) a vertical-mean β retrieved from reflectances averaged over a $(2.2\ \mathrm{km})^2$ area, and (5) a vertical-mean β retrieved using off-nadir reflectances. An asymmetry about nadir in the observed reflectance means and skewnesses is not reproduced by any Monte Carlo simulation. The lack of symmetry can be related to differing proportions of unobscured sunlit and shadowed cloudy areas within the different views, even for these cases with viewing angles close to the perpendicular plane. The Monte Carlo simulations do not appear to capture the observed fraction of unobscured sunlit and shadowed cloudy areas, suggesting that radiatively significant cloud variability is occurring at scales smaller than the height field resolution of ±550 m. Results from the Monte Carlo simulation done at a higher vertical resolution are consistent with this. The cases examined also contain a nadir maximum in the observed reflectance skewnesses and a relative maximum for the observed nadir reflectances, attributed to the solar illumination of some optically thick cloud surfaces and to specular reflection pervading through the optically thin cloudy regions. This contrasts with previous modeling results that assume a Lambertian surface. *INDEX TERMS:* 3359 Meteorology and Atmospheric Dynamics: Radiative processes; 3360 Meteorology and Atmospheric Dynamics: Remote sensing; 3374 Meteorology and Atmospheric Dynamics: Tropical meteorology; 3394 Meteorology and Atmospheric Dynamics: Instruments and techniques; *KEYWORDS:* 3-D radiative transfer, cumulus congestus, MISR

Citation: Zuidema, P., R. Davies, and C. Moroney, On the angular radiance closure of tropical cumulus congestus clouds observed by the Multiangle Imaging Spectroradiometer, *J. Geophys. Res.*, *108*(D20), 4626, doi:10.1029/2003JD003401, 2003.

1. Introduction

[2] Although advances have been made in articulating the three-dimensional radiative transfer effects of many cloud types, one cloud type that remains little explored is cumulus congestus occurring under conditions of enhanced convection. This cloud type can achieve significant optical depths and is inherently complex, a characteristic viscerally appreciated by any aircraft passenger in the Tropics. The very definition of cumulus congestus suggests strong heterogeneity effects: markedly sprouting clouds, often of great vertical extent, with a bulging upper part that frequently resembles a cauliflower [*World Meteorological Organization* (*WMO*), 1956]. Cumulus congestus clouds occur commonly within low-latitude zones. *Johnson et al.* [1999], in their study on the trimodal characteristics of tropical convection, observe that cumulus congestus constituted over half of the precipitating convective clouds sampled by shipboard radar during the Tropical Ocean Global Atmosphere Coupled Ocean Atmosphere Response Experiment (TOGA-COARE).

0148-0227/03/2003JD003401$09.00

[3] The cloud's complexity means that three-dimensional radiative transfer (3DRT) effects may be significant, but they are difficult to quantify. Even the sign of the departure from one-dimensional radiative transfer results is unclear. For example, in cases where solar illumination/shadowing off of the sides of optically thick growing turrets is dominant (radiative ''sharpening''), one-dimensional radiative transfer will overestimate the mean cloud optical depth [e.g., *Várnai*, 2000; *Zuidema and Evans*, 1998]. In contrast, for largely fractured clouds containing both high- and low-optical-thickness regions, large net horizontal photon transports leading to an increased net downward photon transport (radiative ''smoothing'') can dominate, and 1D RT will underestimate the true mean cloud optical depth [e.g., *Chambers et al.*, 1997a].

[4] Previous studies on 3DRT effects come to differing conclusions that depend upon the input cloud representations. Radiative transfer simulations using idealized cloud models both simple and complex can examine a wide range of optical thicknesses and other cloud properties. Such simulations demonstrate the importance of cloud shape, cloud geometry, and spatial arrangement for the top-of-atmosphere reflection [*Davies*, 1978, 1984; *Welch and Wielicki*, 1984; *Breon*, 1992; *Kobayashi*, 1993; *Várnai and Davies*, 1999; *Di Giuseppe and Tompkins*, 2003b; *Várnai and Marshak*, 2001]. In contrast, simulations relying on high-resolution imagery or cloud radar data on broken clouds generate the conclusion that, statistically, net horizontal photon transport is not an important influence on broken cloud domain-averaged fluxes or reflectances [*Chambers et al.*, 1997b; *Benner and Evans*, 2001; *Evans et al.*, 2001]. These studies focus on non-precipitating, all-liquid clouds for which the initial cloud property retrievals are more robust, but the clouds have low optical depth [*Chertock et al.*, 1993]. Another approach is to use output from cloud-resolving models. These 3DRT simulation conclusions become dictated by the uncertain ice microphysical model parameterizations producing the cirrus [e.g., *Emmanuel*, 1994]. If the cirrus fraction is large, the net horizontal photon transport occurring at lower altitudes is small [*Fu et al.*, 2000; *Barker et al.*, 1998, 1999]. Model fields with low cirrus cloud fractions do show significant three-dimensional radiative transfer effects [*Di Giuseppe and Tompkins*, 2003a].

[5] A satellite data-driven approach uses cloud fields initially retrieved from satellite radiance data [e.g., *Chambers et al.*, 1997a, 2001]. The radiance field is realistic, but the retrieved cloud field already contains the three-dimensional effects that are the subject of the study. In addition, shortwave satellite radiance data do not provide enough information to solve for all the unknowns within a three-dimensional cloud reconstruction (i.e., the phase function or asymmetry parameter, the mean single-scattering albedo, and the mean volume extinction coefficient at every single grid box, where mean values are assumed to represent an entire grid box). Toward reducing the number of unknowns, many assumptions must be made regarding cloud phase, the cloud particle size distribution and characteristics, and the vertical distribution of the cloud optical depth. Nevertheless, data-driven radiative transfer simulations of actively convecting clouds are important, despite the problems inherent to the treatment of data on what has been termed ''difficult'' clouds (11th American Meteorological Society Atmospheric Radiation Conference session name). Cloud fields derived from data provide a realistic complexity that modelled cloud representations do not necessarily emulate. Cloud geometry, in particular, is often poorly represented because it is rarely the focus of a cloud modeling study.

[6] The study undertaken here also relies on cloud fields derived from satellite data. It makes the unique contribution that it is able to perform an angular radiance closure, utilizing the multiple viewing angles available with the Multiangle Imaging Spectroradiometer (MISR) [*Diner et al.*, 1999]. Similar to previous studies, the cloud optical depths are first retrieved from the pixel-level nadir radiances using plane-parallel theory (the independent pixel approximation, or IPA). The operational MISR-retrieved cloud heights are used along with different but common assumptions for vertically distributing the optical depth. The impact of the assumptions and of the initial IPA optical depth retrieval upon the simulated radiances can then be assessed with more rigor than is available with single-view satellite measurements. The high number of unknowns preclude a complete evaluation of the cloud radiative behavior, however, the angular radiance closure provides a useful tool toward further elucidating cloud radiative behavior lacking to previous studies [e.g., *Parol et al.*, 1994; *O'Hirok and Gautier*, 1998].

[7] In this initial study, three cloud cases were selected from browse imagery on the basis of a visual examination. They showed a large degree of structure, minimal overlying cirrus, and appeared to contain some optically thick cloudy portions. Cases with low cirrus amount were selected for two reasons. Overlying cirrus will diffuse the solar radiation impinging upon the lower cloud, reducing three-dimensional radiative transfer effects arising from low-order solar scattering. This makes such scenes less interesting for three-dimensional radiative transfer studies. In addition, without independent information about the cirrus ice particle size and habit, the cirrus phase function is not well-known. We sought to minimize this uncertainty within our study. Two of the selected cases can be described as cumulus congestus, and one as deep cumulonimbus. The optical depths were retrieved from the nadir radiances at a solar zenith angle of 20°.

[8] These cases are described further in sections 2 and 3. The cloud reconstruction is described further in section 3, including the microphysical assumptions and the different vertical distributions of the cloud optical depth. The surface albedo and clear-sky characteristics are established from the clear-sky reflectances and are described further in section 4. Section 5 describes the Monte Carlo (MC) model, and in sections 6, 7, and 8 the Monte Carlo radiance simulations are compared to those measured by MISR.

2. Case Description

2.1. MISR

[9] The MISR instrument [*Diner et al.*, 1999], located on the NASA Terra platform, contains nine pushbroom cameras, one positioned at nadir, four facing forward, and four backward, at the viewing angles of ±26.1°, ±45.6°, ±60.0°, and ±70.5°. The instrument has four spectral channels; the 0.67 μm-wavelength radiances, collected at the highest spatial resolution of 275 m, are the data used within this study. The instrument has a swath width of about 360 km,

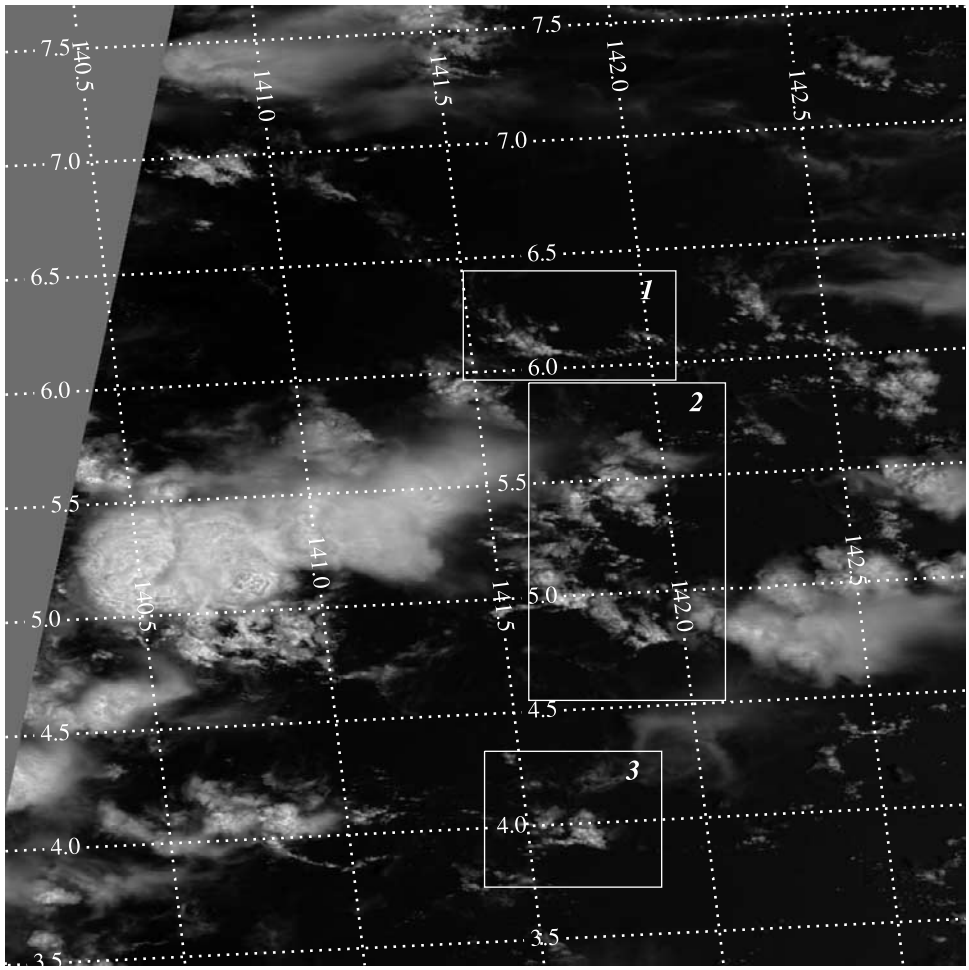

Figure 1. MISR nadir reflectances for 30 September 2001, slightly north of Papua New Guinea. Pixel resolution is 275 m. Latitudes and longitudes are indicated by dashed white lines. White boxes outline the three selected cases and include labels for cases 1, 2, and 3.

and flies in a 705 km polar orbit, with a descending equator-crossing local time of roughly 10:30 A.M.. Approximately seven minutes transpire between the two most oblique views of the same scene. An important implication of the satellite path for this study is that, near the equator, the satellite path is roughly perpendicular to the Sun's principal plane, i.e., the plane formed by the Sun's path within the Sky. Sun glint occurs within the Sun's principal plane, and will most impact the satellite's nadir and near-nadir views.

[10] The radiometric calibration has an absolute uncertainty estimated at within 7%, camera-relative uncertainties within 3%, and pixel-relative uncertainties within 0.5% [*Bruegge et al.*, 2002]. After the research was completed for this paper, an off-axis radiometric calibration error principally affecting the nadir radiances was discovered (C. Bruegge, personal communication, 2002). The error accounted for roughly a 3% increase in the observed nadir radiances, a 1% increase in the near-nadir radiances, and was negligible within the other viewing angles. This error does not affect the paper's conclusions, but its impact is discussed in section 6.

2.2. Sampling Strategy

[11] Near tropical landmasses with coastal mountain ranges, significant convection can occur even at the normally convectively quiescent time of a 10:30 A.M. LT orbit [*Houze et al.*, 1981; *Zuidema*, 2003; *Mapes et al.*, 2003]. The Indonesian maritime continent possesses a substantial shoreline and near-equatorial location, and MISR imagery from this area were examined for suitable cases. The search was confined to the western, less specularly reflecting, side of the orbit.

[12] Figures 1 and 2 show the nadir reflectances and MISR stereo heights, respectively, for the selected orbit portion. The orbit occurred on 30 September 2001, with the equator crossing occurring slightly north of Papua New Guinea (path 101, orbit 9490). The geographical location spans 140°–143°E, 4°–7°N. The orbit registration or correct pixel geolocation for all nine camera views was affirmed by examining an animation composed of the nine camera views of a clear-sky Papua New Guinea land-sea boundary.

[13] Figure 1 shows the domain boundaries of the three selected cases. The most northern case is labeled case 1, with case 2 directly to its south and case 3 the most southern case. Three cases were selected (as opposed to one) to help establish greater generality. Domain boundaries were chosen toward minimizing the atmospheric optical depth at the domain boundaries, but a visual examination of the most oblique views does show a small amount of thin cirrus projected within the static domain boundaries for all three cases.

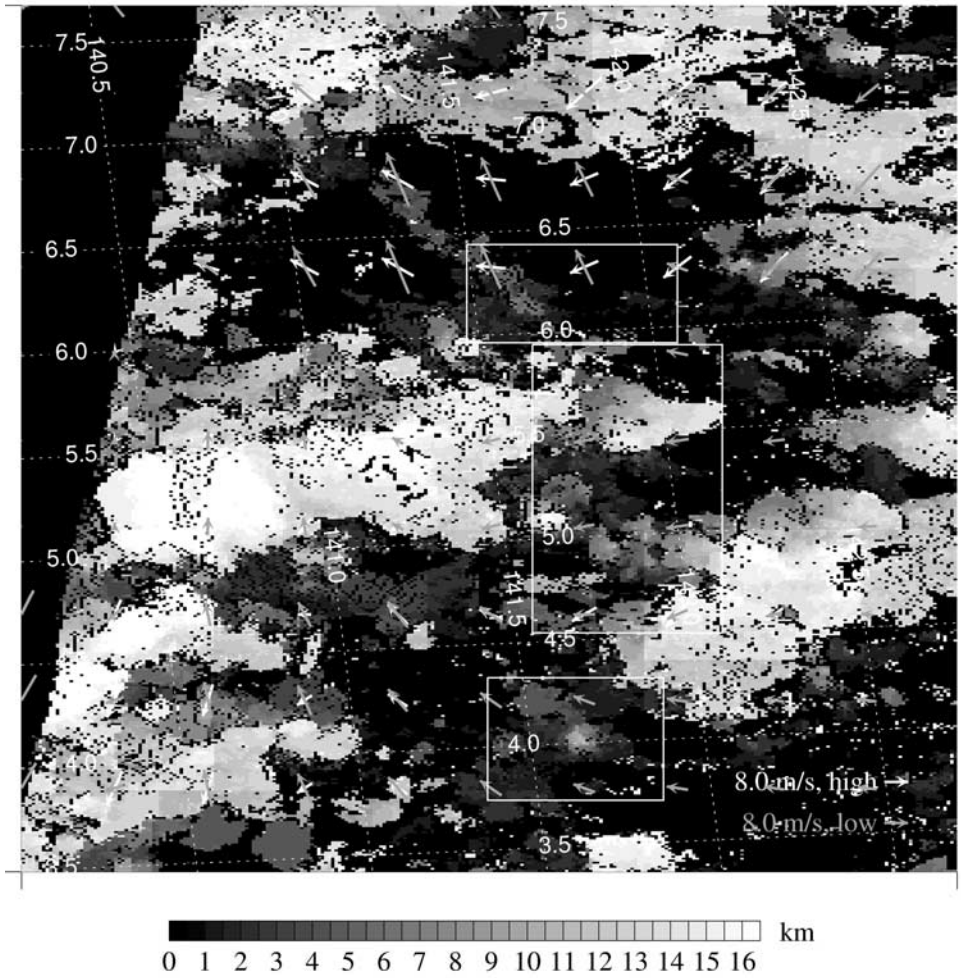

Figure 2. MISR stereo cloud heights. Pixel resolution is 1.1 km. Latitudes and longitudes are indicated by dashed white lines. White boxes outline the three selected cases. White and grey vectors indicate the upper and lower cloud motions. See color version of this figure at back of this issue.

[14] The mean solar zenith and azimuth angle for the selected cases are, respectively, 20° and 293° clockwise from due north (i.e., the Sun is 114° east of due north). The forward and backward (or aft) viewing cameras possess respective azimuth angles of roughly 7° east of north, and 14° west of south (see Figure 9 for a pictorial representation). These angles correspond to azimuth angles relative to the Sun of about 80° for the forward-viewing cameras, so that they experience slightly more forward-scattered sunlight, while the aft-viewing cameras have azimuth angles relative to the Sun of about 115°, so that they experience slightly more backscattered sunlight. Because of the low solar zenith angle, all camera views lie within the backscattering direction: the three nearest-nadir views have scattering angles of 146°–163°, and the most oblique forward and aft views have scattering angles of 105° and 112°, respectively.

3. Cloud Description

3.1. Cloud Height

[15] The MISR cloud heights used within this study are the operationally derived products. The purely geometrical stereo-imaging algorithm first retrieves the cloud-motion vectors (hereafter referred to as winds) using the views from the nadir camera, the most oblique forward- or aft-camera, and the intermediate forward or aft camera with a viewing angle of 45°. After the cloud motion is accounted for, the height is retrieved from the nadir and near-nadir cameras. Previous studies have shown wind errors of about ±3 m s^{-1} [*Horváth and Davies*, 2001] and height errors of about ±560 m [*Moroney et al.*, 2002]. The heights have an inherent resolution of 550 m because of the lack of sub-pixel accuracy in the stereo-matchers. The retrieved cloud height and wind fields are shown in Figure 2. Both fields are continuous across the entire orbit portion, implying a robust wind retrieval (high cirrus that is sometimes visible in the oblique views but not the nadir views is one cause of a discontinuity in tropical wind fields that can then propagate into a discontinuous height field). The MISR cloud-top heights are physically reasonable, with almost no heights occurring above 16.5 km, roughly the location of the tropical tropopause.

[16] An independent comparison with two other data sources was done to increase confidence in the MISR-determined cloud heights. The National Center for Environmental Prediction Reanalysis (NCEP) winds for this location were examined, as well as cloud heights derived

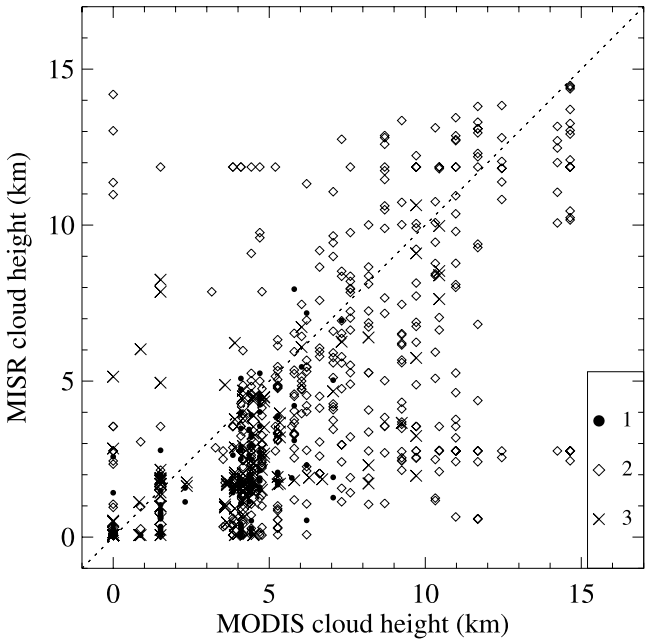

Figure 3. MISR versus MODIS cloud heights, shown as filled circles, diamonds, and crosses for cases 1, 2, and 3, respectively. MISR heights are averaged to match the MODIS 5 km resolution.

from the Moderate Resolution Imaging Spectroradiometer (MODIS) cloud-top temperature data via the mean TOGA-COARE sounding [*Zuidema*, 1998].

[17] The comparison between the MISR and MODIS cloud-top heights for the three cases are shown in Figure 3. The MISR cloud-top heights are generally lower than those for MODIS. A further breakdown by optical depth (not shown) reveals that MISR preferentially senses a lower cloud-top height than does MODIS for the high-optical-depth clouds. A plausible explanation is that the MODIS infrared instrument is responsive to the higher-level cirrus, while the MISR algorithm search for a high short-wave radiance contrast will prefer optically thicker cloud edges that are lower in the atmosphere.

[18] In contrast, for the low-optical-depth clouds, MISR places the cloud tops higher than does MODIS. These are generally cirrus clouds. One explanation may be that the MODIS algorithm is overestimating the infrared emittance of the cloud. Another explanation, supported by an examination of the NCEP winds, is that MISR is using a cloud-motion vector appropriate to the mid-troposphere to estimate cloud heights in the upper troposphere. The NCEP analysis shows eastward winds below about 7.5 km, and strongly westward winds above 12 km, while the MISR algorithm does not retrieve any upper-level westward winds. The MISR winds show agreement with NCEP in other areas, such as wind magnitudes within the MISR error estimate, and a similar meridional shear in clouds at about 6 km or below. This suggests that the MISR wind retrieval is behaving appropriately, but is not sensing the motion of the thin, upper-tropospheric clouds, and is subsequently placing these clouds too high.

[19] The MISR-retrieved cloud heights are utilized within the cloud reconstructions. These cloud reconstructions do not consider multilayered situations, and a MISR algorithm that preferentially places cloud top heights at the (lower) optically thick boundary, is probably appropriate for radiative transfer simulations most interested in the impact of cloud geometry upon the radiance field. The thin upper-level clouds may be placed too high within the atmosphere by the MISR algorithm. Within the radiative transfer simulations, the maximum cloud height is kept at 17 km, reducing this form of error. Nevertheless, the impact of the height error upon the radiative transfer field should be small, as the main impact of thin overlying cirrus will be to diffuse the incoming radiation field, and the actual height is not so relevant as long as the cloud overlies the lower cloud.

3.2. Cloud Optical Depth Estimate

[20] Within this study, plane-parallel optical depth retrievals were performed upon both the nadir view and the backward-viewing (aft) 26° reflectances. The advantage of the nadir view is that cloud sides will be less present, and less likely to be interpreted as cloud top. The disadvantage of the nadir view is the presence of some specular reflection, or "sun glint." The aft 26° view is not affected by sun glint, but cloud sides will be more apparent, and these will be misinterpreted by the plane-parallel optical depth retrieval as cloud top.

[21] The optical depth retrieval was performed using Streamer [*Key*, 2001]. (Another option, appealing for its self-consistency, was to use the Monte Carlo code in a plane-parallel mode. This approach was not used because the Monte Carlo cone-sampling technique strongly affected the simulated nadir reflectances.) This code is a medium-band spectral resolution model, with one band spanning 0.64–0.70 μm, similar to the MISR red band range of 0.655–0.69 μm. Cloud radiation is calculated using a discrete ordinates code (DISORT version 2) with 48 streams (K. Stamnes et al., DISORT, A general-purpose FORTRAN program for discrete-ordinate-method radiative transfer in scattering and emitting layered media: Documentation of methodology (version 1.1), 2000, available at ftp://climate.gsfc.nasa.gov/pub/wiscombe/Multiple_Scatt/). The code was modified to incorporate Mie phase functions with up to 1000 Legendre coefficients. To develop consistency between Streamer, the MISR measurements, and the subsequent Monte Carlo calculations, only Rayleigh scattering was included in the Streamer calculation, and gaseous absorption and aerosols were neglected. Instead, a surface albedo of 0.043 was used to take sun glint and first-order aerosol scattering into account for the Streamer nadir optical depth retrievals. At this surface albedo, the calculated nadir clear-sky reflectance of 0.059 matched that observed by MISR (shown in Figure 6). Similarly, a surface albedo of 0.015 for the aft 26° view matched the observed clear-sky reflectance of 0.032. Occasionally, a low retrieved cloud optical depth coincided with a determination of high-confidence clear conditions by the nadir-view radiometric cloud mask, indicating a difference between the modeled and observed clear-sky reflectance. This may artificially increase the modeled reflectances at the oblique viewing angles.

[22] Lookup tables were constructed for liquid and ice particles separately, using each case's particular viewing and Sun geometry. The composition of clouds with cloud-

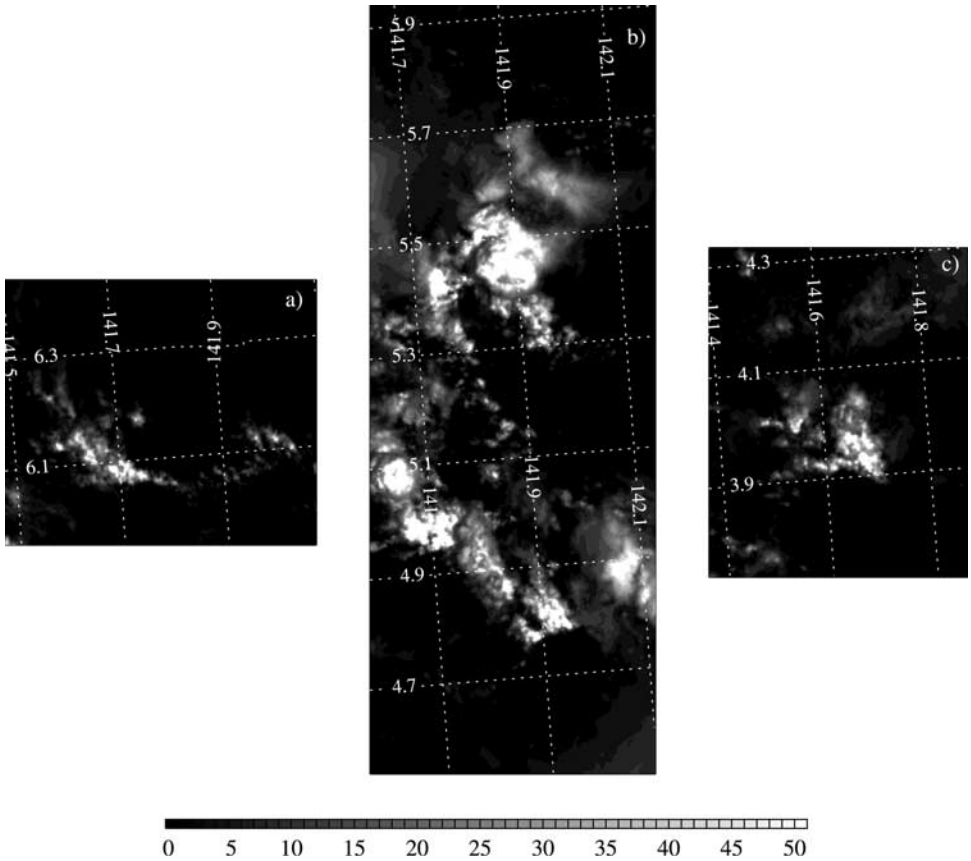

Figure 4. Retrieved optical depths for (a) case 1, (b) case 2, and (c) case 3. See color version of this figure at back of this issue.

top heights at 5.5 km or below was assumed to be entirely liquid water drops with an effective radius of 10 μm and an effective variance of 0.1. The composition of clouds with tops above 11 km was assumed to be spherical ice particles with an effective radius of 30 μm and effective variance of 0.1. At the high nadir view back-scattering angle, the spherical model will slightly overestimate optical depth relative to a regular hexagonal or random-fractal ice particle shape (Figure 4) [*Mishchenko et al.*, 1996]. Most of the focus throughout this paper is on case 3, in part because much of its optical mass is below the freezing level (Figure 5) so that the retrievals and MC simulations are less influenced by the cirrus phase function. Clouds with cloud-top heights in between 5.5 and 11 km were treated as mixed-phase, with the ice and liquid proportion established as a linear function of cloud-top height. This vertical proportioning is plausible

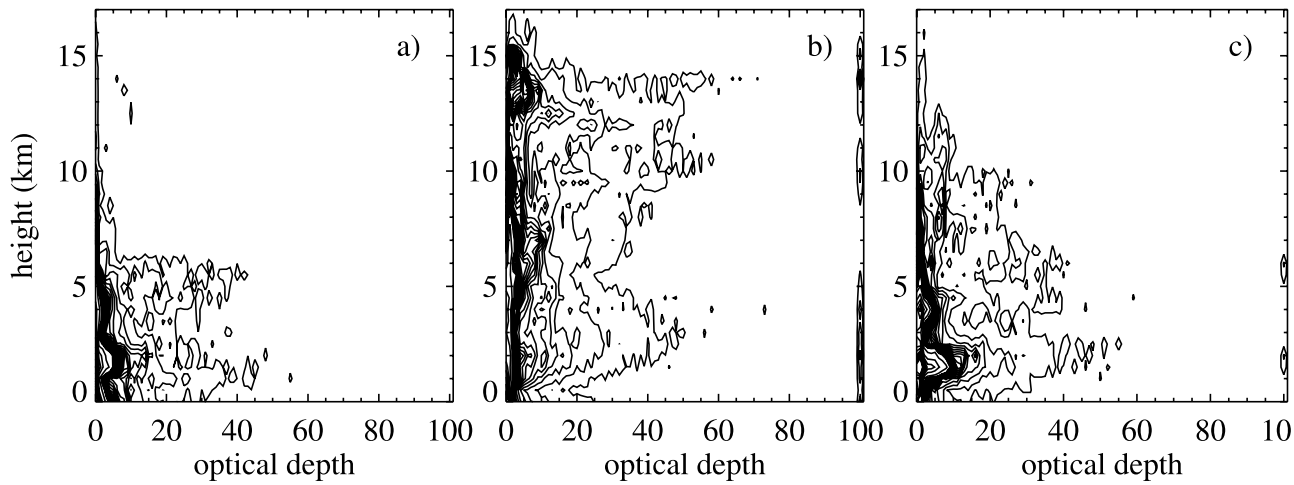

Figure 5. Joint probability distribution for cloud heights and optical depths, for (a) case 1, (b) case 2, and (c) case 3. Contour intervals at 0.02% up to 0.4%, 0.4% up to 4.6%, 20%, and 40%.

Table 1. Cloud Case Characteristics

	Longitude, °E	Latitude, °N	Cloud,[a] %	Mean $H \pm \sigma$,[b] km	Mean Cloud $\tau \pm \sigma$[b]	$\left(\frac{\tau}{\sigma}\right)$[b]	Aspect Ratio, [b]H:W	Domain Size, km^2
1	141.785	6.185	68	1.5 ± 2.0	2.5 ± 6.2	0.16	~0.3	66 × 53
2	141.874	5.225	90	5.5 ± 4.3	7.7 ± 13	0.35	~0.7	61 × 155
3	141.629	4.021	85	2.5 ± 2.1	3.8 ± 7.1	0.28	~0.3	55 × 66

[a]Cloud percentage is determined from the MISR nadir-view radiometric cloud mask.
[b]Here, τ, σ, H, and W denote optical depth, standard deviation, height, and width, respectively.

but arbitrary. A maximum to the retrieved cloud optical depth of 100 was imposed.

[23] Figure 4 shows the retrieved optical depths for the three cases. The figure also shows that case 1 and case 3 consist of one convective element, while case 2 consists of two. The mean optical depth is low for each case (see Table 1), reflecting a large fraction of optically thin cloud material at the cloud edges, but each case contains some high optical depths. The normalized optical depth probability distributions (not shown) for case 1 and case 3 were similar, while case 2 contains a higher proportion of high-optical-depth pixels. These distributions demonstrate a power law form at the low optical depths, becoming exponential at the higher optical depths. As discussed by *Barker et al.* [1996], such optical depth distributions are the most difficult to fit with a gamma distribution function.

[24] Figure 5 shows a joint optical depth and cloud-top height probability distribution for the three cases. The three cases have individually unique bimodal height distributions for the optically thick cloudy portion, suggesting that a parameterization of cloud height based on optical depth, such as proposed by *Minnis et al.* [1992] for convectively suppressed marine clouds, cannot be so readily developed for cumulus congestus. Case 1 and case 3 have optical thickness maxima at 1–2 km and 5 km or slightly higher, while case 2 has optical depth maxima at about 2.5 km and 10 km or slightly higher. The height and optical depth distribution for cases 1 and 3 are consistent with the cumulus congestus description by *Johnson et al.* [1999] of increased cloud detrainment at and above 5 km. Case 1 is the most geometrically and optically thin of the three cases. A summary of the case characteristics is given in Table 1.

3.3. Three-Dimensional Reconstruction

[25] Surface-based ceilometer observations of tropical western Pacific clouds show cloud bases occur most frequently at about 500 m, or slightly above the lifting condensation level of surface air [*White and Fairall*, 1996]. Almost all the cloud bases they observed were within 1 km of the surface. On this basis, a constant cloud-base height of 500 m was assumed within all the three-dimensional cloud field reconstructions. For pixels with a retrieved cloud optical depth but no determined cloud height, a value for the cloud height was interpolated from neighboring pixels.

[26] A minimum extinction of 0.25 km^{-1} was imposed to prevent the placement of an upper-level cirrus cloud base at low altitudes. This means a cloud with its top at 16.5 km must have an optical depth of four or greater to reach the cloud base set at 500 m. The cloud vertical resolution was usually set at 250 m, leaving the cloud-top heights somewhat over-resolved relative to the cloud-top height error of ±550 m. Liquid drop scattering was assumed for cloud material below 5.5 km, spherical ice scattering at heights above 11 km, and a linear weighting by height of liquid and ice scattering at intermediate heights.

4. Clear-Sky Characteristics and Modeling

[27] We developed a surface model for the Monte Carlo model that accounts for ocean surface specular reflection, molecular and aerosol scattering. First, we found a best fit between MISR clear-sky measurements and the analytical model of *Breon* [1993], and then used the *Breon* [1993] model to estimate the clear-sky reflectance at all viewing zenith and azimuth angles. This clear-sky estimate formed the lower boundary condition within the Monte Carlo model; the Monte Carlo model itself does not consider molecular and aerosol scattering, nor the interaction between cloud and clear-sky scattering.

[28] The Breon model accounts for ocean specular reflectance, first- and second-order molecular scattering, specular reflectance combined with molecular scattering, aerosol scattering using a Henyey-Greenstein phase function, and specular reflectance combined with aerosol scattering. The dependence of the ocean glitter pattern upon wind speed and direction was modeled using the *Cox and Munk* [1954] model. Aerosol absorption and white cap ocean reflectance were not included.

[29] First, the MODIS and MISR nadir-view radiometric cloud masks were used to identify clear-sky regions. Then, within these regions, two areas with high spatial homogeneity and minimum radiance values within all nine camera views were selected. These two areas are located slightly north-west of the case 1 region at 142.0–142.07°W, 6.39–6.43°N and 141.8–141.83°W, 6.43–6.45°N; their clear-sky reflectances are shown in Figure 6. The reflectance values do not exceed 7%, demonstrating a low sun-glint contribution. Specular reflection is mostly confined to the nadir view and the forward-viewing +26° camera. The reflectance values differ some between the two regions because of the longitudinal gradient in the glitter reflectance pattern. The standard deviation in the reflectance values, indicated through bars on the mean values, is only detectable for the nadir view.

[30] The modeled values for the views without sun glint (all views excluding the nadir and +26° viewing angles) were iterated until a best fit was found to the observed values. The model results are shown in Figure 7. The full Rayleigh scattering contribution calculated using the Streamer model (open diamonds), and the first and second orders of Rayleigh scattering implemented within the Breon model (dashed line) are shown. Because gaseous absorption is not included in either the Breon or Monte Carlo model,

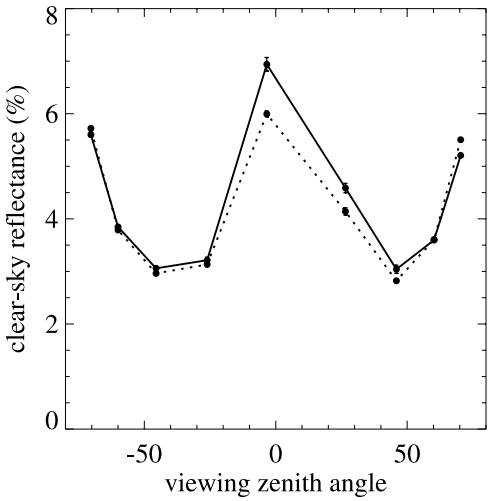

Figure 6. Mean observed clear-sky reflectances for the regions 142.0–142.07°W, 6.39–6.43°N (solid line) and 141.8–141.83°W, 6.43–6.45°N (dotted line). The positive and negative viewing angles correspond to the forward- and aft-viewing cameras, respectively. Error bars are given on the individual measurements, denoting the standard deviation within the domain, and often fall within the size of the filled circle. The relative azimuthal angles range between 80° and 117°.

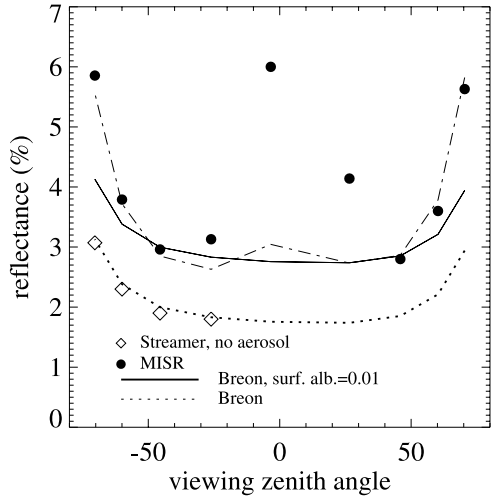

Figure 7. Mean observed clear-sky reflectances for 141.8–141.83°W, 6.43–6.45°N (solid circles), the full Rayleigh scattering contribution calculated by Streamer (open diamonds), the Breon-model first- and second-order Rayleigh scattering contribution without a surface albedo (dotted line) and with a surface albedo of 0.01 (solid line). The Rayleigh optical depth is set to 0.045. Gaseous absorption is not included and is corrected for in the observed values. A Breon model calculation assuming no surface albedo, first- and second-order Rayleigh scattering and an aerosol scattering contribution using an asymmetry factor of 0.75 and an aerosol optical depth of 0.16 is also shown (dot-dash-dot line).

the MISR values were increased by 1/transmittance, with the gaseous transmittance occurring at the MISR red band wavelength evaluated using Streamer. At this wavelength only ozone absorption is considered within Streamer. The gaseous transmittance, deduced from Streamer by calculating radiances with and without a standard McClatchey tropical ozone profile, varied between 0.992 for the nadir view to 0.977 for the most oblique views. (The gaseous absorption line information within Streamer is derived from the Lowtran 3B database [*Selby et al.*, 1976]. Work performed since then [*Burkholder and Talukdar*, 1994] suggests higher ozone absorption coefficient values are more appropriate (A. Horváth, personal communication, 2003).)

[31] In theory, a first-order aerosol scattering contribution can be determined from the backscattered clear-sky reflectances, using a Henyey-Greenstein phase function and assuming no aerosol absorption. An example is shown in Figure 7. When implemented within the Monte Carlo model, however, the radiance contribution from specular reflection combined with aerosol scattering was grossly overestimated within the nadir view. This may reflect an oversampling of the sun-glint pattern by the Monte Carlo solid-angle binning radiance calculation (explained in section 5). For this reason, aerosol was more crudely characterized through an angle-independent surface albedo value of 0.01. This leads to an underestimate of the aerosol contribution to the oblique views (Figure 7).

[32] The Breon model was fitted to the observed reflectances at the sun-glint viewing angles by adjusting the wind speed and wind direction within the Cox-Munk model. The best fit, shown in Figure 8, corresponds to a wind speed of 5.2 m s^{-1} and a wind direction with an angle of 150° relative to the Sun. The fit compares favorably to the NCEP surface wind speed of 7.2 m s^{-1} and less so to the wind direction of 269° relative to the Sun. The clear-sky reflectances subsequently calculated by the Monte Carlo model using the best-fit Breon model as its underlying surface is also shown in Figure 8.

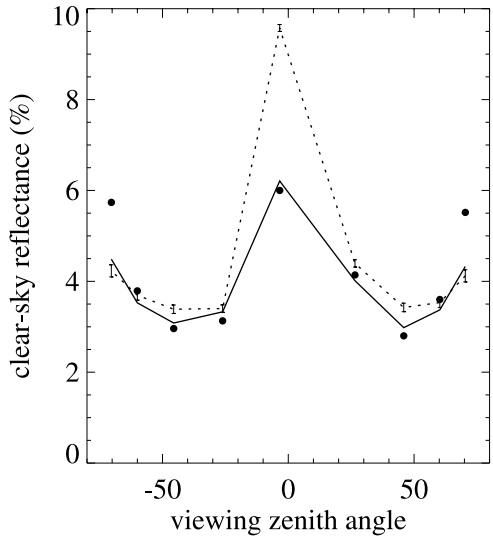

Figure 8. Best fit of the Breon model (solid line) to the observed clear-sky reflectances for 141.8–141.83°W, 6.43–6.45°N (solid circles), along with the corresponding Monte Carlo model clear-sky reflectances (dotted line). The Breon model incorporates the sun glint pattern generated by a wind speed of 5.2 m s^{-1} and a wind direction 3.7° north of east, and a surface albedo of 0.01.

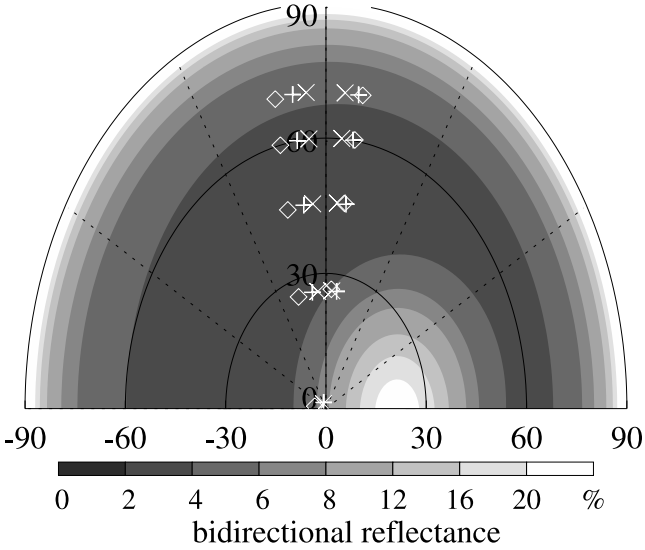

Figure 9. Breon-modeled clear-sky reflectance shown in Figure 8 as a function of viewing zenith angle (radial variable) and relative azimuth angle (angular variable). The forward- and aft-viewing camera viewing angles are shown on the right-hand and left-hand sides, respectively. The solar zenith angle is 20°. White diamonds, plus signs, and crosses indicate the viewing angles of the MISR cameras for cases 1, 2, and 3. The x-axis corresponds to the along-sun plane.

[33] The relationship between the camera viewing angles for all the cases, and the modeled surface reflectance field, are shown in Figure 9. The proximity of the camera viewing angles to the perpendicular plane is made clear. Most theoretical 3D radiative transfer studies have focused on the solar principal plane, where three-dimensional radiative transfer effects from cloud inhomogeneities are most pronounced [*Zuidema and Evans*, 1998; *Várnai*, 2000; *Várnai and Marshak*, 2001]. For our observations, only the nadir camera lies within the principal plane, but in close proximity to the sun-glint region. Most previous simulations utilized a Lambertian surface, thereby neglecting the impact of sun-glint upon cloud reflectance fields.

5. Monte Carlo Model

[34] The forward Monte Carlo (MC) model is an extension of the *Davies* [1978] model. Radiances are calculated by assessing the fluxes entering small solid angle bins ("cone-sampling") with an angular half-width of 8.1° and centered on the MISR-domain-mean viewing zenith and azimuth angles. The cone-sampling method is reliable but averages over details of the angular distribution contained within each cone. In initial experiments using a Lambertian surface, this was most significant for the nadir reflectivity, where a maximum in the photon escape probability occurring exactly at nadir led to a systematic underestimate in the cone-sampled calculated nadir reflectivity. In the experiments with the Breon model acting as the surface, the azimuthal symmetry of the nadir-bin increases its sampling of the specular reflection, with the consequence that the Monte Carlo clear-sky reflectance exceeds the measured value by almost 0.03 for the nadir view (Figure 8).

[35] The same cloud scattering assumed within the Streamer retrieval of optical depth was utilized within the Monte Carlo code: Mie phase functions for liquid and ice particles with effective radii of 10 μm and 30 μm, respectively. The cloud scattering is conservative. The Florida State University combined multiple recursive random number generator was utilized.

[36] Figure 10 compares plane-parallel bidirectional reflectances as calculated by both Streamer and the Monte Carlo code for cloud optical depths of 0.4, 1.0, 2.0, and 4.0. The MC calculation utilizes the Breon model, while the Streamer calculation assumes an angle-invariant surface albedo of 0.043. The impact of the anisotropic surface upon the top-of-cloud reflectances are apparent for cloud optical depths of 2 or less.

[37] Periodic boundary conditions are assumed; the selected domain boundaries are consistent with a weak optical gradient. The Monte Carlo domain-averaged reflectance simulations used 10^7 photons, yielding an uncertainty in the domain-mean reflectances of usually less than 1%, but an unacceptably high pixel-level uncertainty. 10^8 photons were used for calculating the skewnesses (shown in Figure 12). The model can also be run in an independent pixel mode, wherein a photon is not allowed to leave its vertical column. The original *Davies* [1978] model is a participant in the Intercomparison of Three-Dimensional Radiation Codes project (http://climate.gsfc.nasa.gov/I3RC).

[38] The clear-sky model is the largest contributor to the overall model error, as differences exist between the specular reflection within the three cases from that of the clear-sky model. These can amount to ±2% and ±1% for the nadir and +26° viewing angles. Other model error comes from the cone-sampling method (3% model overestimate at nadir and random error within ±0.5% for all angles) and neglect of aerosol (2% model underestimate at the most oblique

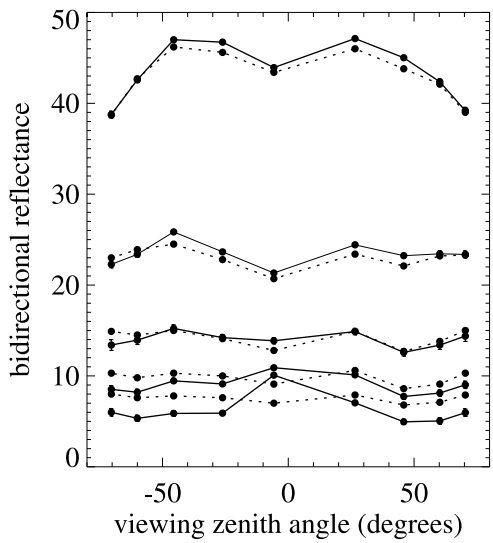

Figure 10. Plane-parallel bidirectional reflectances for optical depths of 0.4, 1, 2, 4, and 10 at the viewing and solar geometry for case 1, as calculated by Streamer (dashed line) and the Monte Carlo model (solid line). The Monte Carlo model utilized the clear-sky model shown in Figure 9, and Streamer used a surface albedo of 0.043.

viewing angles, and random error within ±0.5% for all angles). On the basis of these considerations, we establish total model errors (bias ± random) at viewing zenith angles of −70°, −60°, −45°, −26°, nadir, 26°, 45°, 60°, and 70° of roughly, in percent: −2 ± 1, 0 ± 1, 0 ± 1, 0 ± 1, −3 ± 3, 0 ± 2, 0 ± 1, 0 ± 1, and −2 ± 1.

6. Monte Carlo Reflectance Simulations Using a Vertical-Mean Volume Extinction Coefficient

[39] For these simulations, the optical depth was evenly distributed in the vertical, with a cloud base at 500 m or a minimum volume extinction coefficient (β) of 0.25 km^{-1}. This serves as the reference case.

6.1. Domain-Averaged Means

[40] Figure 11 shows the domain-averaged observed reflectances for the three cases with and without an off-axis radiometric calibration correction, and the reflectances calculated by the Monte Carlo code using a vertical-mean volume extinction coefficient. The total model errors are shown, along with the IPA values for the nadir views. As shown, the impact of including the off-axis radiometric calibration correction within the observed radiances is small.

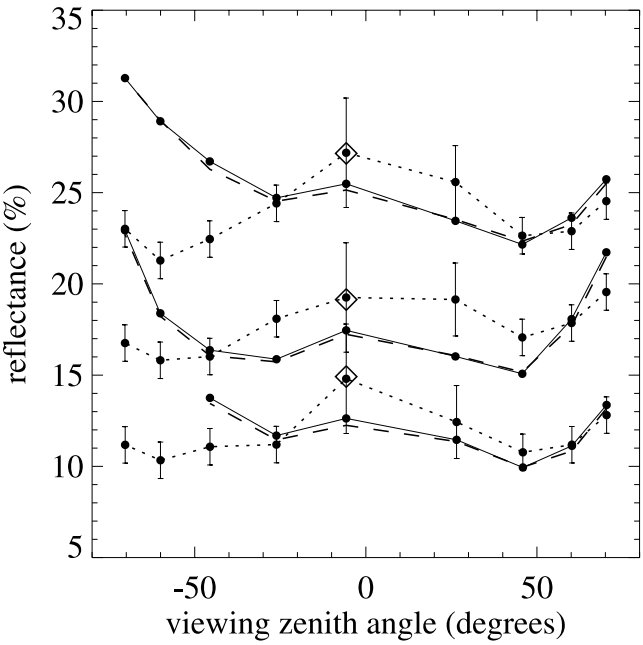

Figure 11. Comparison of domain-averaged Monte Carlo reflectances (dotted line) to the observed values without and with an off-axis radiometric calibration (solid and dashed lines) for the three cases. The negative viewing angles correspond to the aft-viewing cameras, and the positive viewing angles correspond to the forward-viewing cameras. The lowest two lines correspond to case 1, the middle two lines correspond to case 3, and the top two lines correspond to case 2. The nadir MC indepedent pixel reflectances are indicated by diamonds. The measurements for the two most oblique aft-viewing cameras of case 1 contain cirrus and are not depicted. Model errors at each viewing angle are indicated by error bars. These do not include the model bias from the neglect of aerosol at the most oblique viewing angles.

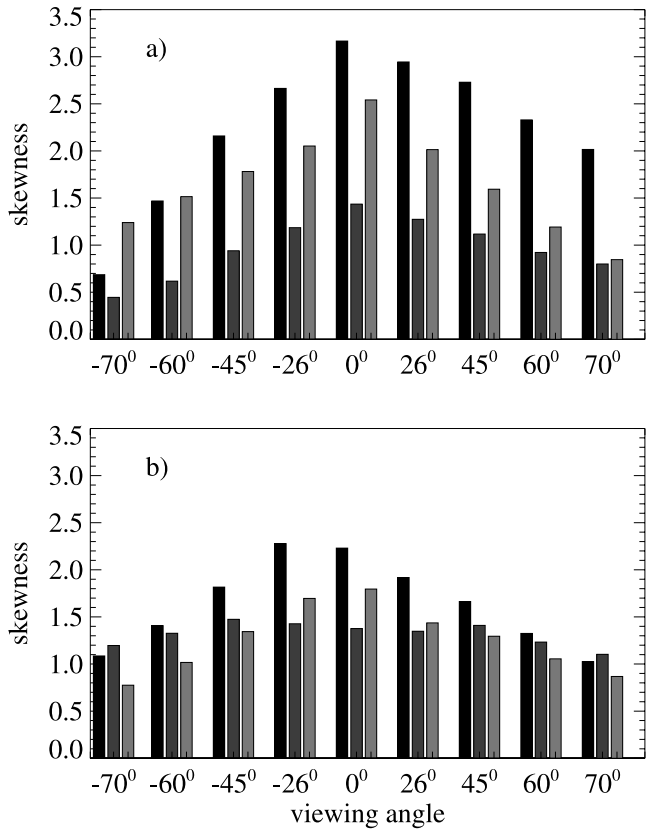

Figure 12. Skewness of (a) observed and (b) Monte Carlo reflectance fields for each of the three cases. Cases 1, 2, and 3 are shown left to right for each of the nine camera angles.

[41] Figure 11 shows observed (MISR) reflectances that are asymmetrical about nadir, with the reflectances from the aft-viewing cameras exceeding those from the forward-viewing cameras. The simulated (MC) reflectances are much more symmetrical about nadir. The Monte Carlo (and IPA) nadir reflectances are higher than the observed nadir reflectances. This is explained by a large number of cloudy pixels with optical depths less than two, so that the Monte Carlo nadir radiance calculation becomes strongly influenced by specular reflection (see Figure 10). The nadir Monte Carlo and IPA reflectances are very close to each other.

6.2. Skewness

[42] A simple yet revealing statistic of the observed and simulated reflectance fields is the skewness, or normalized third moment of a distribution [*Várnai*, 2000]. A large positive skewness is indicative of a large tail of high reflectances. Figure 12 shows the skewness values for the MISR and Monte Carlo reflectances at all nine viewing angles for the three cases.

[43] The skewnesses of the observed reflectances are highest for the nadir view for all three cases, and diminish as the viewing angles become more oblique. The skewness values are also asymmetric about nadir for cases 1 and 2, with the more forward-scattered views (positive viewing

angles) having higher skewness values than the more backscattered views. The Monte Carlo skewnesses do not show these features. The MC skewness values vary much less with viewing angle, with a smaller maximum in the nadir skewness. No asymmetry about the nadir skewness value is evident. These observations are similar to those made previously about the domain-averaged reflectances. Monte Carlo noise is expected to artificially increase the MC skewness values. However, for the nadir and 26° views, the observed values exceed the Monte Carlo values. A comparison between the standard deviation values for the observations and simulations also shows less variability within the simulations than within the observations.

6.3. Discussion

[44] The asymmetry about nadir in the means and skewnesses of the observed cloud reflectances can be interpreted in the following manner. Views at more highly backscattered angles contain more visible sunlit and fewer unobscured shadowed cloudy portions, increasing the overall domain-averaged reflectance and lowering the skewness values. The more forward-scattered views contain a more even mixture of unobscured sunlit and shadowed cloudy areas and are less bright overall while increasing their skewness values. The contrasting Monte Carlo simulations suggest the observed fraction of sunlit and shadowed cloudy areas is not being reproduced. The compensation between sunlit and shadowed areas that occurs within the more forward-scattered views may explain the improved correspondence between the Monte Carlo and MISR views at those angles. The dependence of domain-averaged reflectances on viewing angle for broken modeled clouds is discussed by *Várnai* [2000] for scattering angles falling within the principal solar plane. This study finds observational evidence of the same dependence occurring closer to the perpendicular plane.

[45] A more subtle effect is that the observed domain-mean reflectances show higher values for the nadir view than for the near-nadir view. The observed nadir skewnesses are very high, and a one-dimensional fourier spectra of the observed reflectances (not shown) shows a spectral flattening for the nadir reflectances. The increased variability at smaller spatials is generally associated with the impact of cloud inhomogeneities [*Oreopoulos et al.*, 2000]. A visual inspection of the MISR images reveals the presence of some intensely illuminated cloudy areas within the nadir view. The backscattering angle for the nadir view, which lies within the along-Sun plane, is about 160°. If the illumination effects of bumpy cloud topography exceed the shadowing effects, as might be expected for such a high backscattering angle, an overall increase in the nadir reflectance can occur. While this finding is not particularly surprising, it contrasts with a nadir radiance minimum found in previous studies, attributed to radiative smoothing [e.g., *Zuidema and Evans*, 1998; *Várnai*, 2000; *Chambers et al.*, 2001; *Iwabuchi and Hayasaka*, 2002]. These studies all utilized a Lambertian surface; we produce a similar result when we utilize a Lambertian surface (not shown).

[46] The similarity between the Monte Carlo and IPA nadir reflectances also stands in contrast to previous studies that find lower Monte Carlo nadir reflectances than IPA reflectances, a result of radiative smoothing. The similarity suggests that either these clouds, with their mean height:-width ratios of <0.7, do not have a significantly increased downward photon flux from that of a similar plane-parallel cloud, or, the increased downward photon movement is fully compensated for by brightening from resolved cloud-top bumps.

7. Monte Carlo Reflectance Simulations Using a Vertically Increasing Volume Extinction Coefficient

[47] If the observed nadir reflectances are indeed influenced by solar illumination, an ultimate effect will be that the cloud-top reflectances are poorly correlated with the underlying optical depth distribution, and the optical depths will be poorly retrieved using plane-parallel theory. In this section, two experiments are performed toward elucidating the role of cloud top variability. The first experiment investigates the idea that the near-cloud-top optical mass is underestimated by the use of a vertical-mean extinction coefficient, diminishing the radiative impact of the cloud-top variability within the simulations. Instead, a cloud field is reconstructed assuming an adiabatically vertically increasing volume extinction coefficient (the ''adiabatic experiment''). With this assumption, the liquid water content rises linearly with height, and most of the cloud optical mass is in the upper half of the cloud. The MISR stereo-height algorithm responds to the more optically thick cloud portion (see section 3), so that it is physically reasonable to assume a maximum water content at the MISR-determined cloud top.

[48] Of the three cases, case 3 is the least influenced by overlying thin cirrus in the oblique viewing angles and contains only one convective element of roughly isotropic proportions. Much of its cloud optical mass is in liquid form. It is the only case presented within the remaining simulations.

7.1. Vertically Increasing Volume Extinction Coefficient

[49] The method outlined by *Chambers et al.* [2001] is followed, with the change that the cloud thickness is known, and the parameter A in $L(z) = Az$, where $L(z)$ is the mass of liquid water per unit volume of air, is adjusted so that the optical depth of the column matches the original retrieval. The extinction coefficient depends on height according to $\beta(z) = 2\pi(0.001)[r_e(z)]^2N$, where β, r_e, and N denote the volume extinction coefficient in inverse kilometers, the effective radius in microns, and an assumed number concentration of 100 cm^{-3}, respectively. The effective radius is given by $r_e(z) = \{[3L(z)]/[4\pi\rho_w N]\}^{1/3}$, where ρ_w is the density of liquid water. The assumed droplet distribution has no variance.

[50] Negligible changes were found in the Monte Carlo reflectance simulations corresponding this reconstruction from the vertical-mean extinction coefficient case, and are not shown. This suggests that vertical structure in the volume extinction coefficient alone does not play an important role in determining the top-of-cloud reflectances. This is consistent with previous studies demonstrating that extinction variations have a weaker radiative impact than

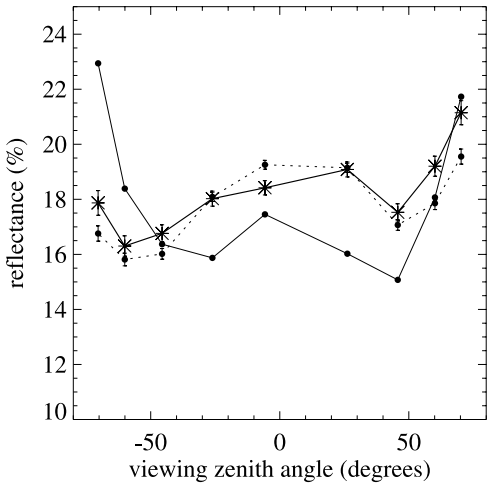

Figure 13. Case 3 Monte Carlo domain-mean reflectances using vertical-mean extinction coefficients at 250 m vertical resolution with the Breon surface model (reference case; dotted line with filled circles), and using adiabatically increasing β at 25 m vertical resolution (solid line with asterisks). The observed domain-averaged reflectances are shown as the solid line with filled circles.

cloud-top variations [*Loeb et al.*, 1998; *Zuidema and Evans*, 1998; *Várnai*, 2000].

7.2. Vertically Increasing Volume Extinction Coefficient at an Increased Vertical Resolution

[51] An expansion of the "adiabatic experiment" tests the idea that cloud structure is underresolved in the simulation at the 250 m vertical resolution. This will be important if the illumination/shadowing effects are occurring at scales smaller than 250 m. A cloud field with increased cloud-top variability is reconstructed through a higher vertical resolution of 25 m and an adiabatically vertically increasing extinction coefficient. This does not imply that the cloud variability is accurate at a 25 m scale, only that it is simulated at that scale.

[52] The corresponding Monte Carlo simulation, shown in Figure 13, differs from the reference case, with the nadir-view reflectances diminished and the reflectances at the oblique views increased. The decrease for the nadir view can be explained as enhanced opportunities for downward photon movement caused by the greater variability. The increase seen for the oblique views can be explained as an increase in the surfaces available for solar illumination.

8. Monte Carlo Reflectance Simulations Using Optical Depth Retrievals at a 2.2-km Spatial Resolution and the 26° Aft-Viewing Reflectances

[53] An additional radiative consequence of radiative sharpening, is that the retrieved domain-averaged optical depth may be overestimated, with the overestimate of the optical depth of illuminated areas outweighing the underestimate of the optical depth of the shadowed areas [*Zuidema and Evans*, 1998; *Várnai and Marshak*, 2002]. This is brought out within a further Monte Carlo experiment, described below, wherein the optical depth is retrieved from reflectances averaged over a $(2.2\ \mathrm{km})^2$ region. The impact of sun glint was also investigated through a simulation using the cloud optical depths retrieved from the aft-viewing 26° camera reflectances. For both simulations, shown in Figure 14, the cloud optical depth was evenly vertically distributed, and the Breon surface model was utilized.

8.1. The $(2.2\ \mathrm{km})^2$ Cloud Optical Depth Retrieval

[54] The optical depths were retrieved from the nadir reflectances averaged over a $(2.2\ \mathrm{km})^2$ spatial scale. The new domain-mean optical depth is 3.5, reduced from the reference case domain-mean value of 3.8. This is consistent with the expectation of radiative sharpening influencing the nadir reflectances. Despite the lower optical depth, an increased domain-averaged reflectance is simulated at all viewing angles. One explanation for this is the increased resemblance to plane-parallel conditions: with less optical depth variability, fewer net photons are encouraged downward.

8.2. Aft-Viewing 26° Cloud Optical Depth Retrieval

[55] A simulation was also performed using the cloud optical depths retrieved from the aft-viewing 26° reflectances. This viewing angle is not affected by sun glint, but the effective cloud fraction is increased through the presence of cloud sides. The mean cloud optical depth for this retrieval is raised slightly to 3.97. For this simulation, the domain-mean nadir reflectance is slightly decreased, and the off-nadir reflectances are slightly increased from that of the reference case. The increase at the off-nadir viewing angles can be attributed to an increase in optical depth associated with the presence of cloud sides. For the nadir view, the decrease in the domain-mean reflectance can be attributed to a smaller number of very bright illuminated cloud surfaces influencing the retrieval, and radiative smoothing can again

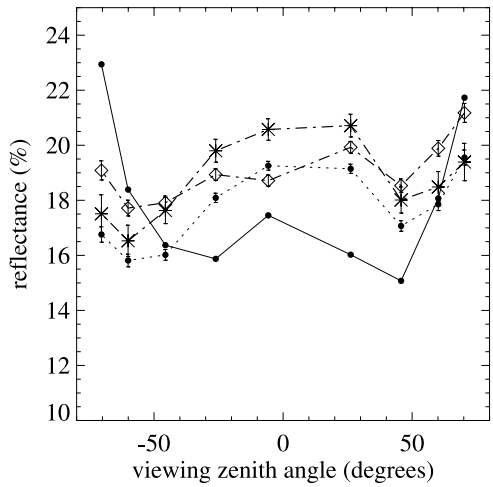

Figure 14. Case 3 Monte Carlo domain-mean reflectances for the reference case (dotted line with filled circles), a simulation using optical depths retrieved from reflectances averaged over a $(2.2\ \mathrm{km})^2$ area (dot-dash line with asterisks), and a simulation using the optical depths retrieved from the aft-viewing 26° reflectances (dot-dash line with diamonds). The observed domain-averaged reflectances are shown as the solid line with filled circles.

become the dominant three-dimensional radiative transfer process. Thus none of the simulations in this or the preceding section capture the angle dependence within the observations.

9. Summary and Concluding Remarks

[56] Monte Carlo simulations of a three-dimensional cloud input representation constructed from MISR imagery were compared to the original reflectances, to assess the IPA retrieval and the assumptions used to determine the cloud vertical structure. The clouds examined were two tropical cumulus congestus and one cumulonimbus cloud field. All three cloud fields have well-defined upper cloud tops with little visible upper-level cirrus outflow. Such clouds are common in tropical convecting regions, are arguably radiatively significant, and have received little previous attention, in part because the quality of a cloud representation derived from conventional satellite data using pixel-scale plane-parallel radiative transfer theory has been difficult to assess. The MISR cloud reconstruction was done at a 275 m spatial resolution and a nominal vertical resolution of 250 m, or a slightly higher resolution than the height-error value of ±550 m. Domain boundaries were established within areas of low cloud optical depth, but did not entirely exclude the presence of neighboring cirrus within the oblique views.

[57] The optical depths were retrieved from the nadir reflectances at a solar zenith angle of 20°. Five Monte Carlo simulations were performed, using differing but common cloud reconstruction assumptions. One simulation used a vertical-mean volume extinction coefficient (β), another used an adiabatically increasing β, a third also used the adiabatic assumption but at a vertical resolution of 25 m, a fourth used the optical depth retrieved from the reflectance averaged over a $(2.2\ \mathrm{km})^2$ area, and the fifth simulation used the cloud optical depths retrieved from the 26° aft-viewing reflectances. All simulations established a cloud base at 500 m and a minimum β of $0.25\ \mathrm{km}^{-1}$.

[58] None of the simulations capture the angle dependence within the observations. An asymmetry about nadir in the observed reflectance means and skewnesses is not evident within the Monte Carlo simulations. Other cases (from the later orbits 17704 and 17748) demonstrated similar behavior in their observed reflectances. The lack of symmetry can be related to differing proportions of unobscured sunlit and shadowed cloudy areas within backscattered and forward-scattered views [*Várnai*, 2000], even for viewing angles close to the perpendicular plane. The Monte Carlo simulations do not capture the observed fraction of sunlit and shadowed cloudy areas. One MC simulation done at a higher vertical resolution supports the idea that radiatively significant cloud variability is occurring at scales smaller than the height field resolution of ±550 m.

[59] The correspondence between the domain-averaged calculated and observed reflectances for all the simulations was most successful for the most geometrically and optically thin case, case 1. Despite this, the modeled and observed reflectance skewness values for case 1 correspond poorly (Figure 12). The apparent inconsistency comes about because the skewness values are strongly influenced by the tail of the reflectance distribution, whereas the domain means are less sensitive.

[60] Higher-order moments such as the reflectance skewness values can serve as valuable indicators of radiative sharpening associated with cloud geometrical variability. The cases we examined showed a nadir maximum in observed reflectance skewnesses and a relative maximum for the observed nadir reflectances. This contrasts with the determination of previous studies that radiative smoothing, a net horizontal photon transport that reduces reflectance variations, is the dominant three-dimensional radiative transfer effect under nadir viewing conditions [*Loeb and Davies*, 1996; *Loeb and Coakley*, 1998; *Loeb et al.*, 1997, 1998; *Zuidema and Evans*, 1998; *Várnai and Marshak*, 2001, 2002; *Iwabuchi and Hayasaka*, 2002]. These previous studies all relied on a Lambertian surface. Instead, our observations and simulations attribute the nadir maximum to the solar illumination of some optically thick cloud surfaces, and to specular reflection pervading through the optically thin cloud edges. The diagnostic value of the skewnesses suggests their use in improving optical depth retrievals, as is also proposed by *Iwabuchi and Hayasaka* [2002].

[61] One weakness of this study is the arbitrarily imposed microphysical parameters (i.e., liquid drops of effective radius 10 μm and spherical ice particles of effective radius 30 μm). As shown by *Mishchenko et al.* [1996], a cirrus phase function calculated from a random-fractal ice particle shape shows higher reflectances than a spherical scattering phase function at the side scattering directions that typify the more oblique viewing angles. Forward radiance calculations using a known cloud representation can link cloud radiative behavior to the underlying cloud properties with more confidence than is possible with cloud fields retrieved from satellite reflectances. For tropical cumulus congestus, the ideal cloud model contains not only realistic cloud microphysics but also realistic small-scale cloud geometry. One example is the modified nested grid version of the Straka Atmospheric Model [*Lasher-Trapp et al.*, 2001, and references therein]. Observed reflectance moment statistics can help assess and improve the suitability of such a cloud model for three-dimensional radiative transfer studies.

[62] **Acknowledgments.** These data were obtained from the NASA Langley Research Center Atmospheric Sciences Data Center. Support received under contract 90486 from the Jet Propulsion Laboratory and a National Research Council Postdoctoral Fellowship is gratefully acknowledged. Akos Horváth is thanked for sharing his insight into the workings of MISR. Iliana Genkova, Darren Jackson, Chris Fairall, and Michael Garay provided thoughtful comments on an earlier draft. Sincere thanks are extended to two anonymous reviewers, whose careful reading and well-considered comments greatly improved the manuscript. Earl Hansen and the MISR reprocessing team are thanked for their prompt reprocessing of MISR orbit 9490. Jeffrey Key is thanked for his generosity in making the radiative transfer model Streamer publicly available through the Website http://stratus.ssec.wisc.edu/streamer/. The FSU random number generator can be found through http://sprng.cs.fsu.edu. The National Center for Environmental Prediction winds were provided by the Climate Diagnostics Center through their website http://www.cdc.noaa.gov/.

References

Barker, H., B. Wielicki, and L. Parker, A parameterization for computing grid-averaged solar fluxes for inhomogeneous marine boundary layer clouds. Part II: Validation using satellite data, *J. Atmos. Sci.*, *53*, 2304–2316, 1996.

Barker, H. W., J.-J. Morcrette, and G. D. Alexander, Broadband solar fluxes and heating rates for atmospheres with 3D broken clouds, *Q. J. R. Meteorol. Soc.*, *124*, 1245–1271, 1998.

Barker, H. W., G. Stephens, and Q. Fu, The sensitivity of domain-averaged solar fluxes to assumptions about cloud geometry, *Q. J. R. Meteorol. Soc.*, *125*, 2127–2152, 1999.

Benner, T. C., and K. Evans, Three-dimensional solar radiative transfer in small tropical cumulus fields derived from high-resolution imagery, *J. Geophys. Res.*, *106*, 14,975–14,984, 2001.

Breon, F.-M., Reflectance of broken cloud fields: Simulation and parameterization, *J. Atmos. Sci.*, *49*, 1221–1232, 1992.

Breon, F.-M., An analytical model for the cloud-free atmosphere/ocean system reflectance, *Remote Sens. Environ.*, *43*, 179–192, 1993.

Bruegge, C., N. Chrien, R. Ando, D. Diner, W. Abdou, M. Helmlinger, S. Pilorz, and K. Thome, Early validation of the Multi-angle Imaging SpectroRadiometer (MISR) radiometric scale, *IEEE Trans. Geosci. Remote Sens.*, *40*, 1477–1492, 2002.

Burkholder, J., and R. Talukdar, Temperature dependence of the ozone absorption spectrum over the wavelength range 410 to 760 nm, *Geophys. Res. Lett.*, *21*, 581–584, 1994.

Chambers, L. H., B. A. Wielicki, and K. F. Evans, Accuracy of the independent pixel approximation for satellite estimates of oceanic boundary layer cloud optical depth, *J. Geophys. Res.*, *102*, 1779–1794, 1997a.

Chambers, L. H., B. A. Wielicki, and K. F. Evans, Independent pixel and two-dimensional estimates of Landsat-derived cloud field albedo, *J. Atmos. Sci.*, *54*, 1525–1532, 1997b.

Chambers, L., B. Wielicki, and N. Loeb, Shortwave flux from satellite-measured radiance: A theoretical study over marine boundary layer clouds, *J. Appl. Meteorol.*, *40*, 2144–2161, 2001.

Chertock, B., C. W. Fairall, and A. White, Surface-based measurements and satellite retrievals of broken cloud properties in the equatorial Pacific, *J. Geophys. Res.*, *98*, 18,489–18,500, 1993.

Cox, C., and W. Munk, Measurements of the roughness of the sea surface from photographs of the Sun's glitter, *J. Opt. Soc. Am.*, *44*, 838–850, 1954.

Davies, R., The effect of finite geometry on the three-dimensional transfer of solar irradiance in clouds, *J. Atmos. Sci.*, *35*, 1712–1725, 1978.

Davies, R., Reflected solar radiances from broken cloud scenes and the interpretation of scanner measurements, *J. Geophys. Res.*, *89*, 1259–1266, 1984.

Di Giuseppe, F., and A. Tompkins, Three-dimensional radiative transfer in tropical deep convective clouds, *J. Geophys. Res.*, *108*, doi:10.1029/2003JD003392, in press, 2003a.

Di Giuseppe, F., and A. Tompkins, Effect of spatial organization on solar radiative transfer in three-dimensional idealized stratocumulus cloud fields, *J. Atmos. Sci.*, *60*, 1774–1794, 2003b.

Diner, D. J., G. P. Asner, R. Davies, Y. Knyazikhin, J.-P. Muller, A. W. Nolin, B. Pinty, C. B. Schaaf, and J. Stroeve, New directions in Earth observing: Scientific applications of multi-angle remote sensing, *Bull. Am. Meteorol. Soc.*, *80*, 2209–2228, 1999.

Emmanuel, K. A., *Atmospheric Convection*, 592 pp., Oxford Univ. Press, New York, 1994.

Evans, K. F., S. McFarlane, and W. Wiscombe, The importance of three-dimensional solar radiative transfer in small cumulus cloud fields derived from the Nauru MMCR and MWR, paper presented at 11th ARM Science Team Meeting, ARM Sci. Team, Atlanta, Ga., 19–23 March 2001.

Fu, Q., M. Cribb, H. Barker, S. Krueger, and A. Grossman, Cloud geometry effects on atmospheric solar absorption, *J. Atmos. Sci.*, *57*, 1156–1168, 2000.

Horváth, A., and R. Davies, Feasibility and error analysis of cloud motion wind extraction from near-simultaneous multiangle MISR measurements, *J. Atmos. Oceanic Technol.*, *18*, 591–608, 2001.

Houze, R. A., S. G. Geotis, J. Marks, and A. West, Winter monsoon convection in the vicinity of North Borneo. Part I: Structure and time variation of clouds and precipitation, *Mon. Weather Rev.*, *109*, 1595–1614, 1981.

Iwabuchi, H., and T. Hayasaka, Effects of cloud horizontal inhomogeneity on the optical thickness retrieved from moderate-resolution satellite data, *J. Atmos. Sci.*, *59*, 2227–2242, 2002.

Johnson, R. H., T. Rickenbach, S. A. Rutledge, P. Ciesielski, and W. Schubert, Trimodal characteristics of tropical convection, *J. Clim.*, *12*, 2397–2418, 1999.

Key, J., Streamer user's guide, 96 pp., Coop. Inst. for Meteorol. Satell. Stud., Univ. of Wisc., Madison, 2001.

Kobayashi, T., Effects due to cloud geometry on biases in the albedo derived from radiance measurements, *J. Clim.*, *6*, 120–128, 1993.

Lasher-Trapp, S., C. Knight, and J. Straka, Early radar echoes from ultragiant aerosol in a cumulus congestus: Modeling and observations, *J. Atmos. Sci.*, *58*, 3545–3562, 2001.

Loeb, N. G., and J. A. Coakley, Inference of marine stratus cloud optical depths from satellite measurements: Does 1D theory apply?, *J. Clim.*, *11*, 215–233, 1998.

Loeb, N. G., and R. Davies, Observational evidence of plane-parallel model biases: Apparent dependence of cloud optical depth on solar zenith angle, *J. Geophys. Res.*, *101*, 1621–1634, 1996.

Loeb, N. G., T. Várnai, and R. Davies, Effect of cloud inhomogeneities on the solar zenith angle dependence of nadir reflectance, *J. Geophys. Res.*, *102*, 9387–9395, 1997.

Loeb, N. G., T. Várnai, and D. M. Winker, Influence of subpixel-scale cloud-top structure on reflectances from overcast stratiform cloud layers, *J. Atmos. Sci.*, *55*, 2960–2973, 1998.

Mapes, B. E., T. T. Warner, and M. Xu, Diurnal patterns of rainfall in northwestern South America. Part III: Diurnal gravity waves and nocturnal convection offshore, *Mon. Weather Rev.*, *131*, 830–844, 2003.

Minnis, P., P. Heck, D. Young, C. Fairall, and J. B. Snider, Stratocumulus cloud properties from simultaneous satellite and island-based instrumentation during FIRE, *J. Appl. Meteorol.*, *31*, 317–339, 1992.

Mishchenko, M. I., W. B. Rossow, A. Macke, and A. A. Lacis, Sensitivity of cirrus cloud albedo, bidirectional reflectance, and optical thickness retrieval accuracy to ice particle shape, *J. Geophys. Res.*, *101*, 16,973–16,985, 1996.

Moroney, C., R. Davies, and J.-P. Muller, Operational retrieval of cloud-top heights using MISR data, *IEEE Trans. Geosci. Remote Sens.*, *40*, 1532–1540, 2002.

O'Hirok, W., and C. Gautier, A three-dimensional radiative transfer model to investigate the solar radiation within a cloudy atmosphere, Part II: Spectral effects, *J. Atmos. Sci.*, *55*, 3065–3076, 1998.

Oreopoulos, L., A. Marshak, R. Cahalan, and G. Wen, Cloud 3D effects evidenced in Landsat spatial power spectra and autocorrelation functions, *J. Geophys. Res.*, *105*, 14,777–14,788, 2000.

Parol, F., J. Buriez, D. Cretel, and Y. Fouquart, The impact of cloud inhomogeneities on the Earth radiation budget: The 14 October 1989 I.C.E. convective cloud case study, *Ann. Geophys.*, *12*, 240–253, 1994.

Selby, J., E. Shettle, and R. McClatchey, Atmospheric transmittance from 0.25 to 28.5 μm, Supplement LOWTRAN 3B, *Environ. Res. Pap. 587*, Air Force Geophys. Lab., Bedford, Mass., 1976.

Várnai, T., Influence of three-dimensional radiative effects on the spatial distribution of shortwave cloud reflection, *J. Atmos. Sci.*, *57*, 216–229, 2000.

Várnai, T., and R. Davies, Effects of cloud heterogeneities on shortwave radiation: Comparison of cloud top variability and internal heterogeneity, *J. Atmos. Sci.*, *56*, 4206–4224, 1999.

Várnai, T., and A. Marshak, Statistical analysis of the uncertainties in cloud optical depth retrievals caused by three-dimensional radiative effects, *J. Atmos. Sci.*, *58*, 1540–1548, 2001.

Várnai, T., and A. Marshak, Observations of three-dimensional radiative effects that influence MODIS cloud optical thickness retrievals, *J. Atmos. Sci.*, *59*, 1607–1618, 2002.

Welch, R., and B. Wielicki, Stratocumulus cloud field reflected fluxes: The effect of cloud shape, *J. Atmos. Sci.*, *21*, 3086–3103, 1984.

White, A. B., and C. W. Fairall, Shipboard measurements of convection during COARE, paper presented at 8th Conference on Air-Sea Interaction, Am. Meteorol. Soc., Atlanta, Ga., 1996.

World Meteorological Organization (WMO), *International Cloud Atlas*, Geneva, 1956.

Zuidema, P., The 600–800-mb minimum in tropical cloudiness observed during TOGA COARE, *J. Atmos. Sci.*, *55*, 2220–2228, 1998.

Zuidema, P., Convective clouds over the Bay of Bengal, *Mon. Weather Rev.*, *131*, 780–798, 2003.

Zuidema, P., and K. F. Evans, On the validity of the independent pixel approximation for boundary layer clouds observed during ASTEX, *J. Geophys. Res.*, *103*, 6059–6074, 1998.

R. Davies and C. Moroney, Jet Propulsion Laboratory, California Institute of Technology, 4800 Oak Grove Drive, Mail Stop 169-237, Pasadena, CA 91109, USA.

P. Zuidema, NOAA Environmental Technology Laboratory, NOAA/ETL/ET6, 325 Broadway, Boulder, CO 80305, USA. (paquita.zuidema@noaa.gov)

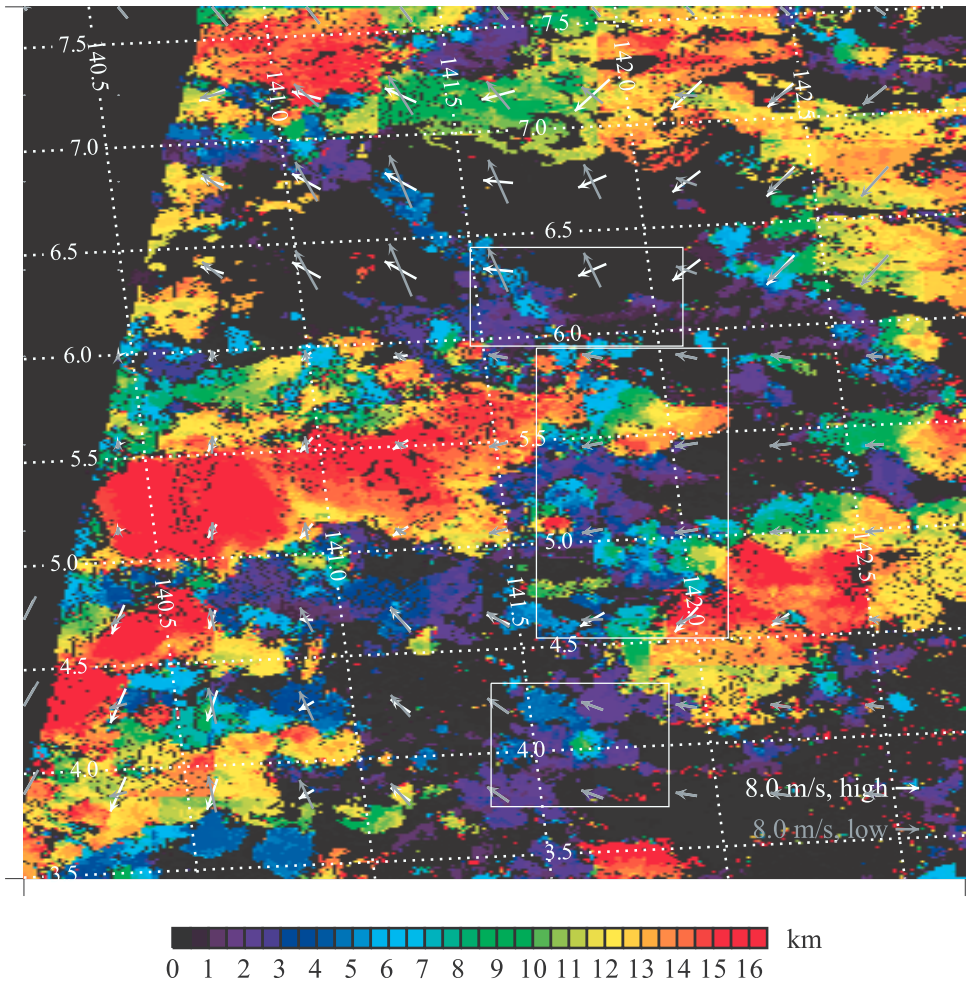

Figure 2. MISR stereo cloud heights. Pixel resolution is 1.1 km. Latitudes and longitudes are indicated by dashed white lines. White boxes outline the three selected cases. White and grey vectors indicate the upper and lower cloud motions.

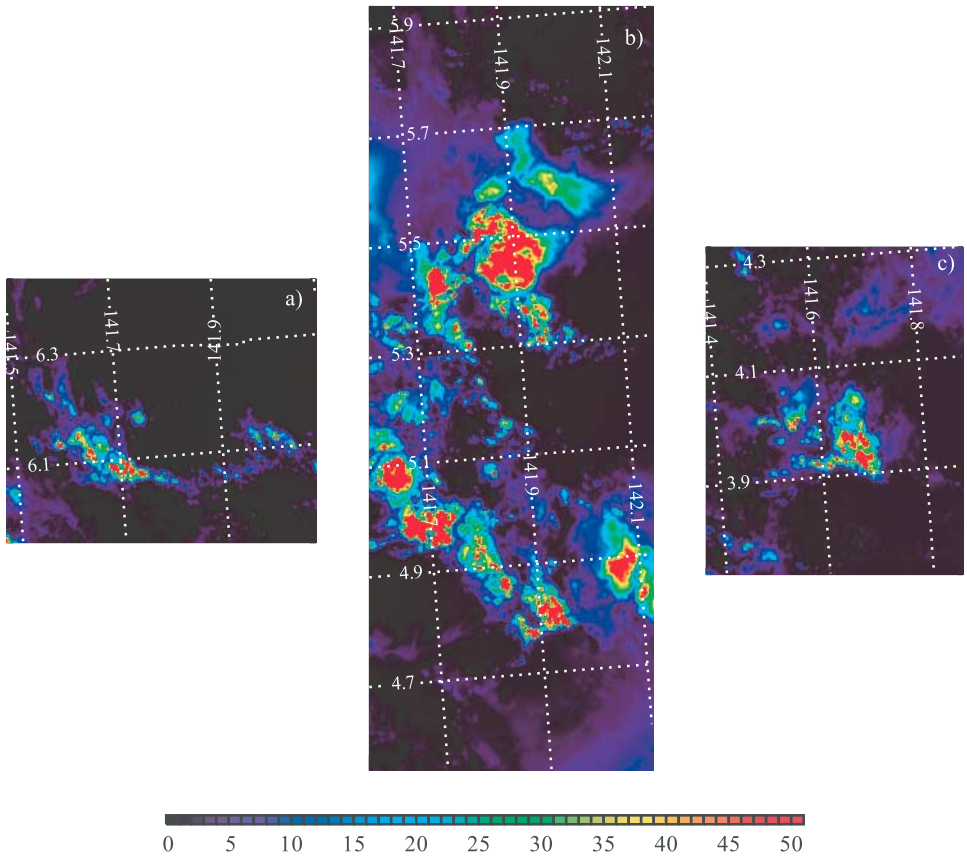

Figure 4. Retrieved optical depths for (a) case 1, (b) case 2, and (c) case 3.